Electrochemical cardiac troponin I immunosensor based on nitrogen and boron-doped graphene quantum dots electrode platform and Ce-doped SnO_2/SnS_2 signal amplification

O. Karaman [a], N. Özcan [b], C. Karaman [c], B.B. Yola [d], N. Atar [e], M.L. Yola [f, *]

[a] Akdeniz University, Vocational School of Health Services, Department of Medical Imaging Techniques, Antalya, Turkey
[b] Iskenderun Technical University, Faculty of Engineering and Natural Sciences, Department of Biomedical Engineering, Hatay, Turkey
[c] Akdeniz University, Vocational School of Technical Sciences, Department of Electricity and Energy, Antalya, Turkey
[d] Iskenderun Technical University, Science and Technology Application and Research Laboratory, Hatay, Turkey
[e] Pamukkale University, Faculty of Engineering, Department of Chemical Engineering, Denizli, Turkey
[f] Hasan Kalyoncu University, Faculty of Health Sciences, Department of Nutrition and Dietetics, Gaziantep, Turkey

ARTICLE INFO

ABSTRACT

The detection of acute myocardial infarction directly depends on the concentration of the cardiac troponin I (CTnI) in human blood plasma. In this study, the sensitive, selective, and fast sandwich-type electrochemical CTnI immunosensor was developed by using nitrogen and boron-dopped graphene quantum dots -as electrode platform and two-dimensional Ce-dopped SnO_2/SnS_2 ($Ce-SnO_2/SnS_2$) as signal amplification. In preparation of electrochemical CTnI immunosensor, the coordinated covalent bond between capture antibody (anti-CTnI-Ab$_1$) and nitrogen and boron-dopped graphene quantum dots as electrode platform led to immobilization of anti-CTnI-Ab$_1$, and the strong esterification between the secondary antibody (anti-CTnI-Ab$_2$) and thioglycolic acid-modified $Ce-SnO_2/SnS_2$ resulted in anti-CTnI-Ab$_2$ conjugation. Finally, the resultant electrochemical CTnI immunosensor was formed via antigen-antibody interaction. High-resolution transmission electron microscopy, X-ray photoelectron spectroscopy, X-ray diffraction, Fourier transform infrared spectroscopy, UV–Vis spectroscopy and Raman spectroscopy, as well as some electrochemical characterization techniques, including cyclic voltammetry, differential pulse voltammetry and electrochemical impedance spectroscopy were used to characterize the prepared immunosensor. The detection limit of CTnI in plasma samples was calculated as 2.00 fg mL^{-1}, making it an effective tool for acute myocardial infarction testing.

1. Introduction

Coronary artery blockage causes cardiovascular disease, which is one of the most severe illnesses for people's health. Acute myocardial infarction (AMI) is a life-threatening illness that has become a primary risk factor for mortality among seniors [1,2]. Therefore, a precise determination of AMI is critical to avoid fatality and morbidity. The I subtype (CTnI), T subtype, and C subtypes of cardiac troponin are regulative proteins for cardiac muscular contractions [3,4]. Once the AMI arises, CTnI is transferred to the circulation for a brief moment, in time without being influenced by other troponin subtypes. Hence, as a specific biomarker, CTnI is

essential in the diagnosis and treatment of AMI [5]. The average concentration of CTnI in healthy people is *ca.*1.25 ng mL^{-1}, whereas the CTnI concentration of more than 2.0 ng mL^{-1} implies an elevated risk of AMI [6,7]. Laboratory test procedures for determining CTnI are precise and trustworthy; however, they are time-consuming, necessitate expert staff, and are not suitable for moment-in-time testing [8,9]. A range of methods for detecting CTnI has recently been proposed, including enzyme-linked immunosorbent assays, chemiluminescence, surface plasmon resonance, fluorescence analysis, and electrochemiluminescence [10–13]. A key priority is the development of a straightforward, practical, and low-cost method for detecting CTnI. Recently, owing to their efficient operation and low reagent consumption, precise and straightforward electrochemical methods used in place of conventional techniques have piqued attention [14–17].

* Corresponding author.
E-mail address: mlutfi.yola@hku.edu.tr (M.L. Yola).

Electrochemical immunosensors are a viable option because of their quick reaction time and ease of scaling, which enables portability. The electrochemical immunosensors, in particular, can effectively accomplish the detection by using straight and particular immunologic intercommunication between the antibody and antigen. All immunosensors rely on the specificity of antigen molecular sensing to achieve a stable pair [18]. Numerous studies have shown that using diverse types of nanostructures (e.g. carbon-based nanomaterials, noble metal nanoparticles, and their nanocomposites) may significantly boost the performance of the electrochemical analysis [19−22]. The morphological structure and particle size distribution of nanomaterials are directly related to the specificity of immunosensors, which are linked to mass transport, as well as biomolecule loading [23].

Graphene quantum dots (GQDs), as zero-dimensional material, is produced from both graphene and carbon dots and are regarded as graphene's small pieces [24,25]. GQDs has important quantum confinement and edge effects similar to carbon dots [24]. In addition, it shows superior properties, such as high biocompatibility, low toxicity, and electrochemical catalysis effect [26]. The doping modification of graphene/GQDs by several atoms such as B, N, Al, and O has been currently confirmed as the effective technique for the modulation of morphological and electronic features of graphene nanosheets in terms of sensor/biosensor applications [27−31]. Especially, B and N atoms have significant attention owing to their atomic size close to C atom. It is concluded that B and N atoms' electron acceptor and donor properties can produce p-type and n-type graphene, respectively [30,32,33]. In addition, nitrogen and boron-dopped graphene type materials demonstrate tunable properties with respect to the doping sites [34,35].

Sn-based composites present superior biological compatibility, high catalysis performance, and low toxicity for catalytic applications, such as biomolecule and environmental pollution detections [36,37]. These composites are generally composed of tin, sulfur, and oxygen. Nonetheless, single-atom Sn-based compounds, including SnS_2 and SnO_2, offer limited electric conversion efficiency. As a result of the formation of heterostructures, electron/hole separation may be achieved, suggesting enhanced both usage range and catalytic efficiency [38].

Herein, in the light of all aforementioned points in mind, the goal of this work is to establish a state-of-art electrochemical cardiac troponin I immunosensor relied on nitrogen and boron-dopped graphene quantum dots (N−B-GQDs) and Ce−SnO_2/SnS_2 for the first time in literature. The fabricated immunosensor provides a number of benefits, including ease of use, speed, and selectivity. Moreover, a precise LOD of 2.00 fg mL^{-1} was observed with high selectivity and no interference in plasma samples. Hence, the proposed electrochemical cardiac troponin I immunosensor paws the way for developing a novel approach in the early-stage detection of possible cardiac disorders.

2. Materials and methods

2.1. Materials

CTnI, anti-CTnI monoclonal capture antibody (anti-CTnI-Ab$_1$), anti-CTnI monoclonal secondary antibody (anti-CTnI-Ab$_2$), myoglobin (MYG), bovine serum albumin (BSA), cardiac troponin T (cTnT), 3-aminophenyl boronic acid monohydrate (3-ABAM), hydrogen peroxide (H_2O_2), Ce(NO$_3$)$_3$·6H$_2$O, SnCl$_4$·5H$_2$O, thioacetamide, thioglycolic acid (TGA), N-(3-dimethylaminopropyl) (EDC) and N-hydroxysuccinimide (NHS) were supplied from Sigma-Aldrich. As a supporting electrolyte and diluting buffer solution, a 0.1 M phosphate-buffered saline (PBS) solution (pH = 7.0) were used.

2.2. Apparatus for evaluation of nanomaterials

Surface morphological characteristics were explored by using a JEOL 2100 TEM. X-ray patterns of nanomaterials were recorded by a Rigaku X-ray diffractometer with Cu−K radiation (λ = 0.150 nm). The PHI 5000 Versa Probe spectrometer was used to perform the XPS survey. FTIR, UV−Vis and Raman measurements were performed by Jasco FTIR Spectrometer, Mettler Toledo and LabRam HR Raman Spectrometer, respectively. Electrochemical characterization methods including CV, EIS and DPV were also conducted via the Gamry Reference 600 workstation (Gamry, USA).

2.3. Synthesis of N−B-GQDs

First, the dissolution of 3-ABAM (0.10 g) was prepared in acetone (50.0 mL) under strong stirring. After that, H_2O_2 (10.0 mL) was introduced into the as-obtained solution. Followed by the ultrasonication of this dispersion, it was transferred into a Teflon stainless autoclave and heated to 240 °C. The product was dialyzed for 10 days using a molecular porous membrane after cooling to room temperature. Afterward, **N−B-GQDs** was collected and dried at 25 °C [39].

2.4. N−B-GQDs-modified glassy carbon electrode (N−B-GQDs/ glassy carbon electrode) as electrochemical sensor platform with anti-CTnI-Ab$_1$ and CTnI immobilizations

The glassy carbon electrode (GCE) was prepared as follows to be used in the further steps [40]. First, 0.1 μm and 0.05 μm Al$_2$O$_3$ slurries were transferred on cleaning pads, respectively. Following, the GCE were polished with these alumina slurries for 20 min. Subsequently, the electrodes were rinsed with isopropyl alcohol and acetonitrile, respectively, to remove the alumina remains at 25 °C. The electrode modifications with N−B-GQDs suspension (10.0 μL, 0.1 mg mL^{-1}) were performed by dropping the suspension on the clean GCEs. After 20 min, the solvent removal was carried out by an infrared heat lamp, providing N−B-GQDs modified GCEs (**N−B-GQDs/GCE**). Anti-CTnI-Ab$_1$ (20.0 μL, 20.0 μg mL^{-1}) was introduced drop wise onto the surface of N−B-GQDs/GCE, providing **anti-CTnI-Ab$_1$/N−B-GQDs/GCE** via the coordinated covalent bond at 37.0 °C for 20 min. Following that, BSA (3.0% w/v) was incubated on anti-CTnI-Ab$_1$/N−B-GQDs/GCE at 37.0 °C for 20 min to eliminate the non-specific interactions (**BSA/anti-CTnI-Ab$_1$/N−B-GQDs/GCE**). Various CTnI proteins were incubated to BSA/anti-CTnI-Ab$_1$/N−B-GQDs/GCE for 20 min (**CTnI/BSA/anti-CTnI-Ab$_1$/N−B-GQDs/GCE**). Finally, non-contacting CTnI proteins were eliminated via interfacing the prepared CTnI/BSA/anti-CTnI-Ab1/N−B-GQDs/GCE with 0.1 M PBS (pH 7.0).

2.5. Preparation of Ce−SnO_2/SnS_2 and TGA-modified Ce−SnO_2/SnS_2

A facile one-step hydrothermal production technique was used for the synthesis of Ce−SnO_2/SnS_2. With this regard, the mixture of Ce(NO$_3$)$_3$·6H$_2$O (0.30 mmol) and SnCl$_4$·5H$_2$O (5.0 mmol) was prepared in ultra-pure water (40.0 mL) under stirring for 20 min. Subsequently, thioacetamide (8.0 mmol) was gently introduced into the previous solution for 10 min. The solution was then placed into a Teflon stainless autoclave, and the thermal annealing was conducted at 200 °C for 20 h. After the cooling to the ambient temperature, **Ce−SnO_2/SnS_2** was collected via centrifugation at 5000 rpm, following it was rinsed with ethanol several times, and as-obtained **Ce−SnO_2/SnS_2** was dried at 25 °C [41].

Finally, the dispersion of Ce−SnO_2/SnS_2 (10.0 mmol, 20.0 μL) was treated with TGA solution (20.0 mmol, 20.0 μL) and stirred for 20 min,

providing TGA-modified Ce−SnO$_2$/SnS$_2$ via [Sn−S−CH$_2$−COOH] (**TGA/Ce−SnO$_2$/SnS$_2$**).

2.6. TGA-modified Ce−SnO$_2$/SnS$_2$ signal amplification with anti-CTnI-Ab$_2$ conjugation

The mixture (10.0 μL) of EDC/ N-hydroxysuccinimide dispersion (1:1, v/v) was interacted with TGA/Ce−SnO$_2$/SnS$_2$ (10.0 μL, 10.0 mg mL^{-1}) to activate −COOH groups on TGA/Ce−SnO$_2$/SnS$_2$. Then, the binding of anti-CTnI-Ab$_2$ (20.0 μL, 20.0 μg mL^{-1}) to TGA-modified Ce−SnO$_2$/SnS$_2$ was performed by interaction between −COOH of TGA-modified Ce−SnO$_2$/SnS$_2$ and −NH$_2$ of anti-CTnI-Ab$_2$ via strong ester bond, providing **anti-CTnI-Ab$_2$/ Ce−SnO$_2$/SnS$_2$** [42].

2.7. Electrochemical measurements

The dispersion of anti-CTnI-Ab$_2$/Ce−SnO$_2$/SnS$_2$ (20.0 μL, 20.0 mg mL^{-1}) was dropped on CTnI/BSA/anti-CTnI-Ab$_1$/N−B−

GQDs/GCE electrode surface at a 20 min immunological response time. The fabricated electrochemical immunosensor was tagged as **Ce−SnO$_2$/SnS$_2$/anti-CTnI-Ab$_2$/CTnI/BSA/anti-CTnI-Ab$_1$/N−B-GQDs/ GCE** and stored in 0.1 M PBS (pH 7.0, 5.0 mL) at 25 °C. Before the electrochemical measurements, high purity Ar gas (99.999%) was circulated through the electrochemical cell for 10 min to remove dissolved oxygen and eliminate corrosive effects. The voltammograms were acquired at 25 °C in an isolated cabinet with no pressure fluctuations to avoid the external ambient effects. For monitoring the electrochemical performance toward CTnI, the potential ranging from +0.0 to +0.3 V was applied to 1.0 mM H$_2$O$_2$ solution. Scheme 1 showed the preparation procedure of electrochemical CTnI immunosensor, including the preparations of electrode platform and signal amplification.

2.8. Processing of samples

Sample preparation process was detailed on Supplementary Data [43].
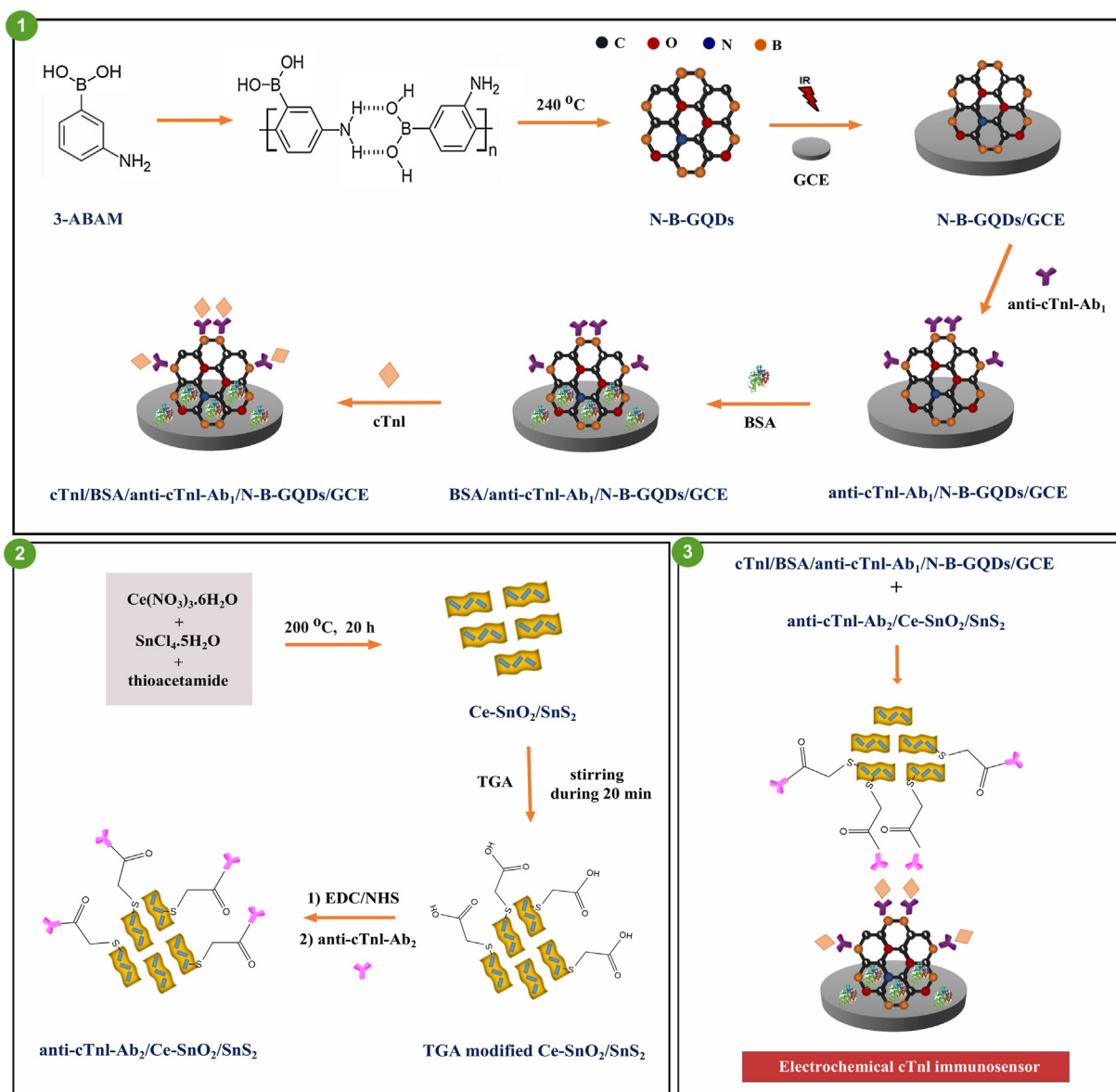
Scheme 1. Schematic illustration of the fabrication procedure of electrochemical CTnI immunosensor.

3. Results and discussion

3.1. Fundamental of electrochemical immunosensor based on N−B-GQDs and Ce− SnO$_2$/SnS$_2$

3-ABAM, H$_2$O$_2$, and acetone were used as a precursor, an oxidizing agent, and a solvent, respectively, for the preparation of N−B-GQDs at 240 °C via a two-step reaction. In the first step, the incorporation of 3-ABAM monomers into macromolecules was performed; thanks to the hydrogen bonds formed between the amino and boric acid groups. Afterward, the bonds between carbon and hydrogen of phenyl rings on macromolecules were broken off for the generation of nitrogen and boron-doped carbon-based free radicals, following larger carbon-based fragments at higher temperatures because of acetone's gasification. Thus, the decomposition of H$_2$O$_2$ into O$_2$, H$_2$O, and free radicals such as HO• and HOO• occurred. The improved pressure by O$_2$ and H$_2$O formed the crystallization of carbon-based fragments, providing N−B-GQDs formation. O$_2$ also reacted with N−B-GQDs, resulting in inner vacancy defects [44] and free radicals reacted with N−B-GQDs, resulting in hydrophilic groups, providing N−B-GQDs' dispersibility. Furthermore, the octet gap in the boron atom led to the formation of stable chemical structures with biomolecules, including unpaired electrons; thanks to the coordinated covalent bond [45]. In sensor platform development, N−B-GQDs as Lewis acid with electron deficiency via boron atoms and anti-CTnI-Ab$_1$ as Lewis base with unbound electron pairs via −NH$_2$ groups formed anti-CTnI-Ab$_1$/N−B-GQDs by the coordinated covalent bond.

Ce−SnO$_2$/SnS$_2$ as a signal amplification was prepared by a facile one-step hydrothermal production technique. The valance and conduction band levels of SnO$_2$ and SnS$_2$ indicated the ladder pattern, suggesting a strong contact interface [46]. Owing to Ce doping, the electron transfer and electron-hole pairs recombination occurred, providing the improvement of electrochemical activity. Then, the strong esterification between anti-CTnI-Ab$_2$ and TGA-modified Ce−SnO$_2$/SnS$_2$ via −NH$_2$ and −COOH groups provided a highly stable and conductive anti-CTnI-Ab$_2$/Ce−SnO$_2$/SnS$_2$. Finally, H$_2$O$_2$ was used as a redox probe in this work because of its easy oxidation into O$_2$ and continuous monitoring [47,48].

3.2. Characterizations of N−B-GQDs

The TEM micrograph of N−B-GQDs provided in Fig. 1A offered a mean particle size of 4−5 nm. The inset of Fig. 1A presenting the high-resolution transmission electron microscopy (HR-TEM) image suggested that the N−B-GQDs with a highly crystalline structure belonging to an interplanar distance of about 0.211 nm, attributing to (100) lattice planes of graphene [49]. Atomic force microscopy (AFM) image (Fig. 1B) proved that the height of N−B-GQDs was to be 1.8 nm and the thickness of about 0.65−0.75 nm [50]. Hence, the preparation of N−B-GQDs with 2 or 3 layers was successfully achieved in this work. XRD (Fig. 1C) and Raman spectrum (Fig. 1D) were obtained for the determination of crystallographic structure and phase purity. XRD peak at 18.9° corresponded to 002 plane of bulk graphite. Raman spectrum confirmed the high degree of graphitization, suggesting the stronger G band at 1579 cm^{-1} than the D band at 1349 cm^{-1} (the peak intensity ratio is about 2.0) [51]. The existence of defects in N−B-GQDs was also verified via D-band [52,53].

Fig. 2A showed XPS survey, confirming O1s, N1s, C1s, and B1s on N−B-GQDs. According to the N1s spectrum (Fig. 2B), the peaks at 397.1 eV and 399.1 eV corresponded to pyridinic nitrogen. Moreover, the peaks that appeared at ca.399.8 eV and 401.8 eV were attributed to pyrrolic and quaternary nitrogen, respectively [54]. B1s spectrum (Fig. 2C) showed three XRD peaks attributing to C−B at 190.4 eV, C=B at 192.1 eV and O−B−C at 193.8 eV [39]. The peaks
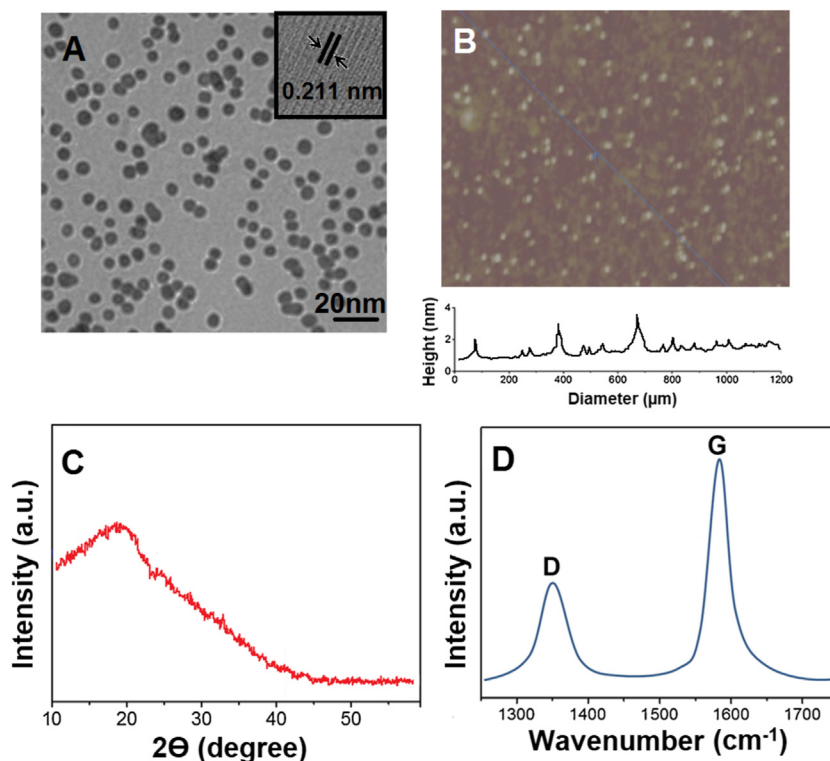

Fig. 1. (A) TEM image of N−B-GQDs (Inset: the lattice fringe of an N−B-GQD), (B) AFM image of N−B-GQDs, (C) XRD pattern and (D) Raman spectrum of N−B-GQDs. N−B-GQDs, nitrogen and boron-doped graphene quantum dots; TEM, transmission electron microscopy; XRD, X-ray diffraction.
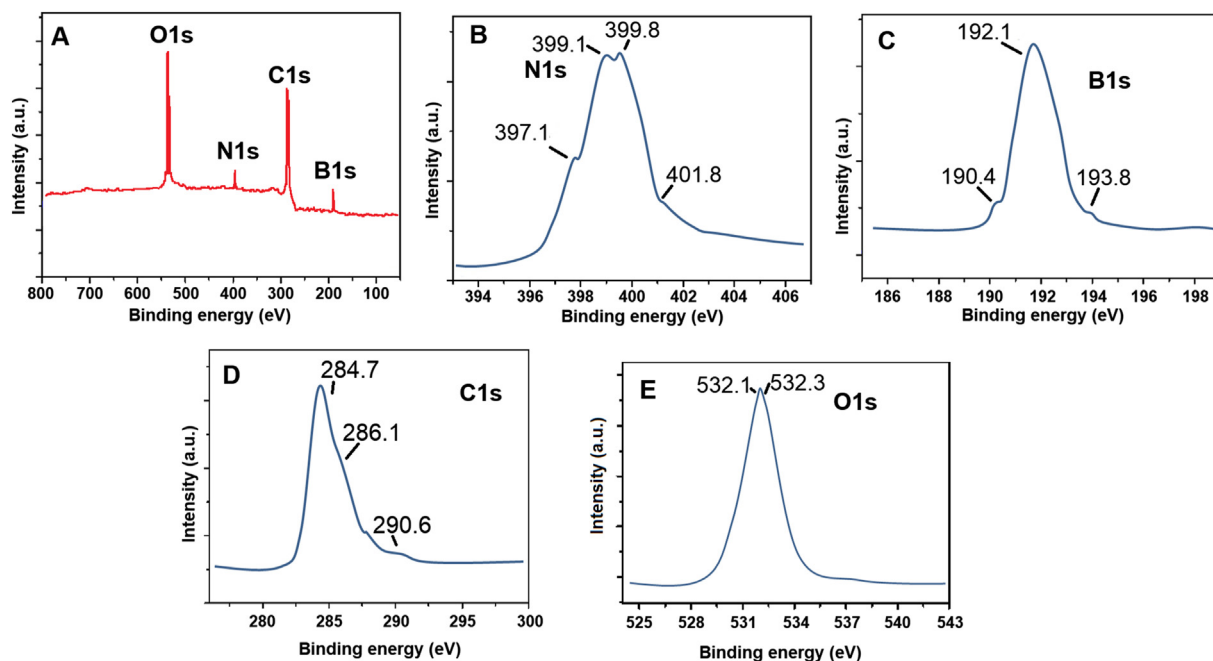
Fig. 2. (A) XPS survey of N−B-GQDs and high-resolution XPS spectrum of (B) N1s, (C) B1s, (D) C1s, and (E) O1s. N−B-GQDs, nitrogen and boron-doped graphene quantum dots; XPS, X-ray photoelectron spectroscopy.

at 284.7, 286.1, and 290.6 eV were ascribed to the C−C/C═C, C−O, and O−C═O groups, respectively, as per C1's high-resolution XPS survey (Fig. 2D) [55]. Moreover, the peaks at 532.1 and 532.3 eV were detected in the high-resolution O1s spectra (Fig. 2E), which were attributed to CO and C−OH groups, respectively [56].

FTIR spectrum (Fig. S1A) was also acquired for N−B-GQDs. The absorption bands at 1710 cm^{-1} and 3440 cm^{-1} were ascribed to the carboxylic acid's C═O stretching and OH groups, respectively. The hydrophilic groups on N−B-GQDs, such as −COOH, was expected to provide the nanomaterial to be water-soluble. In addition, N−B-GQDs' surface charge (Fig. S1B) was calculated to be −16.8 mV, resulting from hydrophilic groups' presence. Moreover, the UV−Vis spectra (Fig. S2A) was obtained for N−B-GQDs and two absorption peaks at 270 nm and 309 nm were observed. The absorption peak at 270 nm corresponded to n-π* transition of C═O, whereas the peak at 309 nm was ascribed to the specific absorption of GQDs [57]. A

wide absorption peak ranging between 600 nm and 900 nm was attributed to the conjugated system, including delocalized electrons in N−B-GQDs [58]. In addition, several excitation wavelengths were used to gather photoluminescence spectra of N−B-GQDs, and N−B-GQDs exhibited an excitation wavelength and upconverted fluorescence (Fig. S2B and C) [39]. According to the results, the distribution of emission intensity and peak position varied with wavelength.

3.3. Characterizations of Ce−SnO₂/SnS₂

According to Fig. S3 of Ce−SnO₂/SnS₂, SnO₂/SnS₂, SnO₂ and SnS₂, the specific XRD peaks at 14.82°, 28.17°, 31.89°, 50.17° and 52.49° attributing to (001), (100), (101), (110) and (111) lattice planes of tetragonal structure, respectively, confirmed the presence of SnS₂ (curve d). Curve c of Fig. S3 showed a hexagonal phase of SnO₂, in
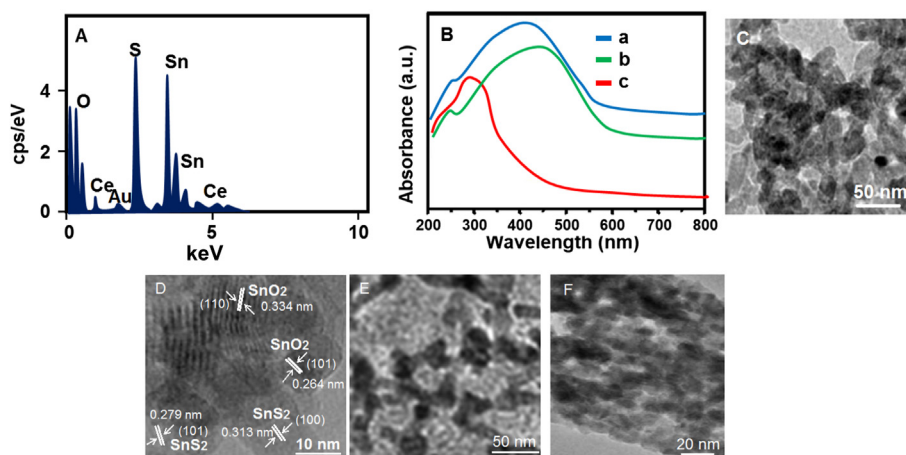

Fig. 3. (A) EDX image of Ce−SnO₂/SnS₂, (B) UV−Vis spectra of Ce−SnO₂/SnS₂ (spectrum a), SnS₂ (spectrum b) and SnO₂ (spectrum c), (C) TEM and (D) HR-TEM images of Ce−SnO₂/SnS₂, TEM images of (E) SnS₂ and (F) SnO₂. HR-TEM, high-resolution transmission electron microscopy; TEM, transmission electron microscopy; UV−vis, ultraviolet visible.
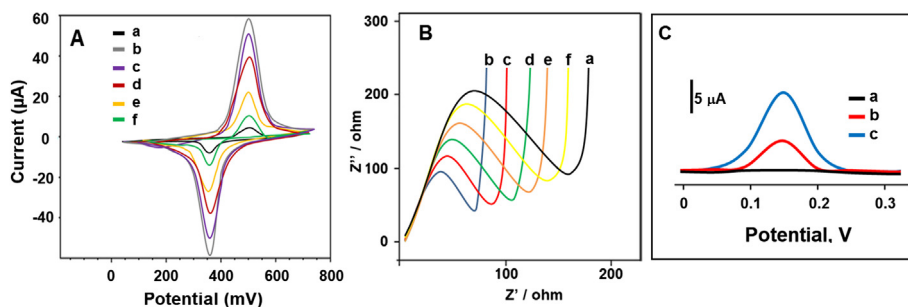
Fig. 4. (A) Cyclic voltammograms, (B) EIS responses at (a) bare GCE, (b) N−B−GQDs/GCE, (C) anti-CTnI-Ab₁/N−B−GQDs/GCE, (D) BSA/anti-CTnI-Ab₁/N−B−GQDs/GCE, (E) CTnI/BSA/ anti-CTnI-Ab₁/N−B−GQDs/GCE, (F) the final immunosensor including c-anti-CTnI-Ab₁, CTnI and anti-CTnI-Ab₂ (scan rate of 50 mV s⁻¹) in 1.0 mM [Fe(CN)₆]³⁻ containing 0.1 M KCl and (C) DPV responses of the proposed immunosensors incubated with 0.500 pg mL⁻¹ CTnI using anti-CTnI-Ab₂/SnO₂/SnS₂ (curve b) and anti-CTnI-Ab₂/Ce−SnO₂/SnS₂ (curve c) in absence of H₂O₂ (curve a) and in presence of 1.0 mM H₂O₂. BSA, bovine serum albumin; DPV, differential pulse voltammetry; GCE, glassy carbon electrode; EIS, electrochemical impedance spectroscopy; N−B−GQDs, nitrogen and boron-doped graphene quantum dots.

which the peaks detected at 26.54°, 34.17°, 38.24°, 52.19° and 66.19° was attributed to (100), (101), (200), (211), (112) lattice planes. Curve a and curve b verified the presence of SnO_2/SnS_2, providing the successful synthesis of nano-heterostructure. Finally, it was realized that due to the modest doping of Ce on the nano-heterostructure, the divergence between curves a and b was minor. However, according to the energy dispersive x-ray (EDX) image (Fig. 3A), the presence of O, S, Sn, and Ce elements confirmed the successful dopping tretament of Ce on nano-heterostructure. Fig. 3B demonstrated UV−Vis spectra of $Ce−SnO_2/SnS_2$, SnS_2 and SnO_2. There were weak absorption bands of SnO_2 and SnS_2 in comparison with $Ce−SnO_2/SnS_2$, indicating the improved absorption capacity of $Ce−SnO_2/SnS_2$. TEM image (Fig. 3C) of $Ce−SnO_2/SnS_2$ showed the rod type nano-heterostructure. According to Fig. 3E and F, the large pieces, including in SnO_2 and SnS_2, were observed. Finally, HR-TEM image (Fig. 3D) of $Ce−SnO_2/SnS_2$ indicated the lattice spaces, including 0.313, 0.279, 0.334, and 0.264 nm, corresponding to (100), (101) of SnS_2 and (110), (101) of SnO_2, respectively [41].

Fig. S4A showed XPS survey, providing the presence of Ce, O, S, and Sn elements on $Ce−SnO_2/SnS_2$. Furthermore, the peaks detected at *ca.*886.8 eV, 902.1 eV, and 918.2 eV were attributed to Ce^{3+} 3d5/2, Ce^{4+} 3d3/2, and Ce^{4+} 3d3/2 states, respectively (Fig. S4B) [59]. On the other hand, the peaks at 161.2 eV and 162.2 eV corresponded to S^{2-} 2p3/2 and S^{2-} 2p1/2, respectively, confirming sulfur presence (Fig. S4C) [60]. In addition, O^{2-} 1s binding energy at 531.4 eV was attributed to oxygen element in SnO_2 (Fig. S4D). Finally, XPS peaks at 485.7 eV and 495.1 eV were attributed to Sn^{4+} 3d5/2 and Sn^{4+} 3d3/2, respectively. Hence, the preparation of $Ce−SnO_2/SnS_2$ was successfully accomplished (Fig. S4E).

3.4. Evaluation of electrochemical performance of the sensor platform and signal amplification

The evaluation of the electrochemical performance of the as-prepared sensor platform was progressively performed, by using CV and EIS methods in the presence of 1.0 mM $[Fe(CN)_6]^{3-/4-}$ as redox pair. First, the anodic and cathodic signals on bare GCE were observed at Epa = 500 mV and Epc = 350 mV, respectively, (curve a of Fig. 4A). As expected, when N−B−GQDs/GCE was used, the increased electrochemical sensor signals were observed because of GQDs' quantum confinement and edge effects [61,62] (curve b of Fig. 4A). Nonetheless, the anti-CTnI monoclonal capture antibody (anti-CTnI-Ab₁)'s blocking effect resulted in the decreases in anodic and cathodic signals (curve c of Fig. 4A). To confirm the successful anti-CTnI-Ab₁ immobilization, SEM image (Fig. S5) of anti-CTnI-

Ab₁/N−B−GQDs/GCE demonstrating a spherical size and agglomeration was obtained, providing a successful immobilization of anti-CTnI-Ab₁. After the immobilizations of BSA (curve d of Fig. 4A) and CTnI (curve e of Fig. 4A), respectively, the gradual decreases on anodic and cathodic signals were obtained owing to more electron transfer blocking. Thus, it is concluded that the immobilization treatments of BSA and CTnI on electrode surfaces were successfully carried out. In the case of the utilization of the final immunosensor (curve f of Fig. 4A), a further decrease in sensor signals was observed due to the more antibody-CTnI interactions. EIS measurements confirmed CV results in the immunosensor development process (Fig. 4B). The obtained charge transfer resistances were calculated as 190 Ω for bare GCE (curve a), 90 Ω for N−B−GQDs/GCE (curve b), 110 Ω for anti-CTnI-Ab₁/N−B−GQDs/GCE (curve c), 130 Ω for BSA/anti-CTnI-Ab₁/N−B−GQDs/GCE (curve d), 150 Ω for CTnI/BSA/anti-CTnI-Ab₁/N−B−GQDs/GCE (curve e) and 170 Ω for the final immunosensor, respectively. Thus, it was concluded that the preparation procedure of the immunosensor was completed successfully based on CV and EIS results.

For electrochemical performance characterization (Fig. 4C) of the prepared signal amplification, several immunosensors using anti-CTnI-Ab₂/SnO₂/SnS₂ (curve b) and anti-CTnI-Ab₂/Ce−SnO₂/
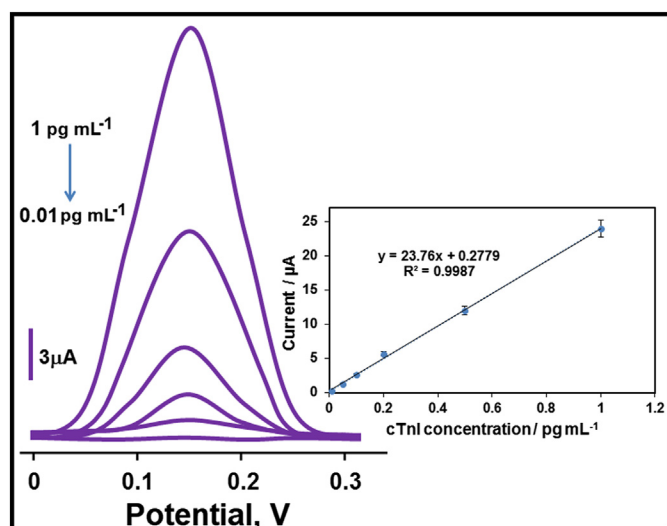

Fig. 5. Concentration effect (from 0.01 to 1.0 pg mL⁻¹ CTnI) on immunosensor signals, Inset: Calibration curve for electrochemical CTnI immunosensor (Potential range is +0.0/+0.3 V; Parameters are frequency of 100 Hz, pulse amplitude of 25 mV and scan increment of 5 mV).

Table 1
The comparison of electrochemical CTnI immunosensor with the other novel techniques.

Method	Linear Range	LOD	Ref.
Electrochemiluminescence	$100.00\ fg\ mL^{-1} - 20.00\ ng\ mL^{-1}$	$43.00\ fg\ mL^{-1}$	[64]
Electrochemical	$10.00\ fg\ mL^{-1} - 100.00\ ng\ mL^{-1}$	$3.02\ fg\ mL^{-1}$	[65]
Electrochemical	$0.01-100.0\ ng\ mL^{-1}$	$3.0\ pg\ mL^{-1}$	[7]
Photoelectrochemical	$0.01\ pg\ mL^{-1} - 1.00\ ng\ mL^{-1}$	$3.00\ fg\ mL^{-1}$	[66]
Electrochemiluminescence	$0.01-1000.0\ pg\ mL^{-1}$	$5.01\ fg\ mL^{-1}$	[67]
Electrochemiluminescence	$5.00\ pg\ mL^{-1} - 20.00\ ng\ mL^{-1}$	$3.20\ pg\ mL^{-1}$	[68]
Photoelectrochemical	$0.001-100.0\ ng\ mL^{-1}$	$0.30\ pg\ mL^{-1}$	[69]
QCM	$25.00\ pg\ mL^{-1} - 15.00\ ng\ mL^{-1}$	$18.0\ pg\ mL^{-1}$	[70]
Electrochemical immunosensor	$\mathbf{0.01 - 1.00\ pg\ mL^{-1}}$	$\mathbf{2.00\ fg\ mL^{-1}}$	**This study**

SnS_2 (curve c) were fabricated by 0.50 pg mL^{-1} CTnI at the immune reaction time of 20 min, and DPV signals were recorded in 1.0 mM H_2O_2. The optimal and highest electrochemical signals were observed by using Ce−SnO_2/SnS_2. Because of cerium's good catalytic activities and its superior chemical and electronic properties, the obvious electrocatalytic activity on sensor signals was obtained [63]. In addition, because of the strong esterification bond between anti-CTnI-Ab$_2$ and TGA-modified Ce−SnO_2/SnS_2, stable electrochemical signals were provided by using the developed electrochemical immunosensor in this study.

3.5. Optimization for electrochemical measurements

The influences of the solution pH, immune reaction time, H_2O_2, and anti-CTnI-Ab$_2$/Ce−SnO_2/SnS_2 solution concentrations were evaluated and detailly presented in Fig. S6.

3.6. Linearity range

The calibration equation by using CTnI concentrations and the electrochemical immunosensor signals was y = 23.76x + 0.2779, with a correlation coefficient of R^2 = 0.9987, here, y and x stand for the current (μA) and CTnI concentration (pg mL^{-1}), respectively (Fig. 5). The quantification limit and LOD were found to be 0.01 pg mL^{-1} and 2.00 fg mL^{-1}, respectively. The comparisons between the prepared electrochemical CTnI immunosensor and the other new detection methods were tabulated in Table 1. According to the findings, it can be speculated that the ultra-sensitive and selective CTnI immunosensor was first presented in the literature, providing early detection of significant cardiovascular diseases in a shorter time. In contrast to conventional CTnI detection techniques,

the removal of time-consuming steps in CTnI immunosensor preparation allows for portable application. In addition, the production of fast immunosensor signals resulted in efficient analysis in a shorter time. Finally, the immunosensor preparation with the minimal waste generation showed that the prepared immunosensor was friendly to the environment and human health. Hence, the developed stable and reproducible electrochemical CTnI immunosensor may offer a potential for early cardiovascular detection.

3.7. Recovery

The recovery experiments including plasma samples were performed by the prepared electrochemical CTnI immunosensor. The close to 100.00% values suggested the high selectivity of the electrochemical immunosensor, providing the successful CTnI analysis without interference effect (Table S1). Furthermore, the standard addition method was applied to plasma samples and y = 24.09x + 10.0963, with R^2 = 0.9993 was obtained as a calibration equation. Hence, we can say that the close slope values between direct calibration (inset of Fig. 5) and standard addition methods confirmed the high selective CTnI analysis.

3.8. Selectivity, stability, and reproducibility

For the selectivity assessment, several electrochemical CTnI immunosensors were fabricated by using various target dispersions, such as (i) 100.0 pg mL^{-1} MYG + 100.0 pg mL^{-1} BSA + 100.0 pg mL^{-1} cTnT, (ii) 0.500 pg mL^{-1} CTnI + 100.0 pg mL^{-1} MYG, (iii) 0.500 pg mL^{-1} CTnI +100.00 pg mL^{-1} BSA, (iv) 0.500 pg mL^{-1} CTnI + 100.00 pg mL^{-1} cTnT. Afterward, these electrochemical immunosensors were applied to 1.0 mM H_2O_2 solution. Fig. 6A confirmed that the prepared electrochemical immunosensor was able to provide high selectivity toward CTnI protein. Moreover, Fig. 6B demonstrated the stability test of the prepared electrochemical immunosensor for 7 weeks. It was determined that the final immunosensor signals were about 99.08% of the first electrochemical signal, providing the high stability of the immunosensor. Finally, for the reproducibility test, 25 identical electrochemical CTnI immunosensors were prepared separately by the same protocol described in sections 2.4, 2.6, and 2.7. The relative standard deviation of 0.93 was calculated by using the observed 25 electrochemical signals, confirming the high reliability of the immunosensor production procedure.

Fig. 6. (A) Immunosensor selective responses against the prepared solutions (n = 6), (i) 100.0 pg mL^{-1} MYG + 100.0 pg mL^{-1} BSA + 100.0 pg mL^{-1} cTnT, (ii) 0.500 pg mL^{-1} CTnI + 100.0 pg mL^{-1} MYG, (iii) 0.500 pg mL^{-1} CTnI +100.0 pg mL^{-1} BSA, (iv) 0.500 pg mL^{-1} CTnI + 100.00 pg mL^{-1} cTnT; (B) Stability test of electrochemical CTnI immunosensor, including 0.500 pg mL^{-1} CTnI (n = 6) at 25.0 °C. BSA, bovine serum albumin; MYG, myoglobin.

4. Conclusions

Herein, highly selective and sensitive electrochemical cardiac troponin I immunosensor based on N−B-GQDs as electrode platform and 2D Ce-doped SnO_2/SnS_2 as signal amplification was presented. The developed electrochemical immunosensor was
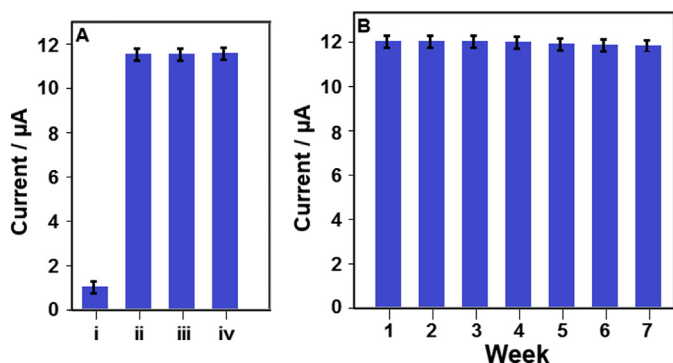
fabricated via the coordinated covalent bond between capture antibody-N—B-GQDs, and the strong esterification between secondary antibody-Ce-doped SnO_2/SnS_2. Hence, the stable electrochemical signals were accomplished in terms of early cardiovascular detection. Moreover, the prepared immunosensor was reproducible biosensor and did not include time-consuming steps, such as sensor preparation. Finally, it can be speculated that the proposed immunosensor can be easily integrated into a commercial biosensor tool and used to diagnose AMI.

Credit author statement

Onur KARAMAN: Conceptualization, Methodology, Writing - review & editing. **Nermin ÖZCAN:** Data curation, Visualization, Investigation. **Ceren KARAMAN:** Data curation, Visualization, Investigation. **Bahar BANKOGLU YOLA**: Data curation, Visualization, Investigation. **Necip ATAR**: Writing - original draft, Visualization, Investigation. **Mehmet Lütfi YOLA**: Supervision, Conceptualization, Writing - review & editing.

Declaration of competing interest

The authors declare that they have no known competing financial interests or personal relationships that could have appeared to influence the work reported in this paper.

Acknowledgment

Appendix A. Supplementary data

Supplementary data related to this article can be found at https://doi.org/10.1016/j.mtchem.2021.100666.

References

[1] M. Abdorahim, M. Rabiee, S.N. Alhosseini, M. Tahriri, S. Yazdanpanah, S.H. Alavi, et al., Nanomaterials-based electrochemical immunosensors for cardiac troponin recognition: an illustrated review, Trac. Trends Anal. Chem. 82 (2016) 337—347.

[2] M. Reiter, R. Twerenbold, T. Reichlin, P. Haaf, F. Peter, J. Meissner, et al., Early diagnosis of acute myocardial infarction in the elderly using more sensitive cardiac troponin assays, Eur. Heart J. 32 (2011) 1379—1389.

[3] V.K. Gupta, B. Sethi, R.A. Sharma, S. Agarwal, A. Bharti, Mercury selective potentiometric sensor based on low rim functionalized thiacalix [4]-arene as a cationic receptor, J. Mol. Liq. 177 (2013) 114—118.

[4] P. Nandhikonda, M.D. Heagy, An abiotic fluorescent probe for cardiac troponin I, J. Am. Chem. Soc. 133 (2011) 14972—14974.

[5] S.S. Wang, Y.Y. Zhao, M.M. Wang, H.J. Li, M. Saqib, C.H. Ge, et al., Enhancing luminol electrochemiluminescence by combined use of cobalt-based metal organic frameworks and silver nanoparticles and its application in ultrasensitive detection of cardiac troponin I, Anal. Chem. 91 (2019) 3048—3054.

[6] G.Z. Liu, M. Qi, Y. Zhang, C.M. Cao, E.M. Goldys, Nanocomposites of gold nanoparticles and graphene oxide towards an stable label-free electrochemical immunosensor for detection of cardiac marker troponin-I, Anal. Chim. Acta 909 (2016) 1—8.

[7] S.Y. Cen, X.Y. Ge, Y. Chen, A.J. Wang, J.J. Feng, Label-free electrochemical immunosensor for ultrasensitive determination of cardiac troponin I based on porous fluffy-like AuPtPd trimetallic alloyed nanodendrites, Microchem. J. 169 (2021) 106568.

[8] B. Rezaei, A.M. Shoushtari, M. Rabiee, L. Uzun, W.C. Mak, A.P.F. Turner, An electrochemical immunosensor for cardiac Troponin I using electrospun carboxylated multi-walled carbon nanotube-whiskered nanofibres, Talanta 182 (2018) 178—186.

[9] D. Brondani, J.V. Piovesan, E. Westphal, H. Gallardo, R.A.F. Dutra, A. Spinelli, et al., A label-free electrochemical immunosensor based on an ionic organic molecule and chitosan-stabilized gold nanoparticles for the detection of cardiac troponin T, Analyst 139 (2014) 5200—5208.

[10] J. Ye, L.P. Zhu, M.X. Yan, Q.J. Zhu, Q.Q. Lu, J.S. Huang, et al., Dual-wavelength ratiometric electrochemiluminescence immunosensor for cardiac troponin I detection, Anal. Chem. 91 (2019) 1524—1531.

[11] J.F. Masson, L. Obando, S. Beaudoin, K. Booksh, Sensitive and real-time fiber-optic-based surface plasmon resonance sensors for myoglobin and cardiac troponin I, Talanta 62 (2004) 865—870.

[12] S.K. Srivastava, V.K. Gupta, S. Jain, Determination of lead using a poly(vinyl chloride)-based crown-ether membrane, Analyst 120 (1995) 495—498.

[13] S.M. Seo, S.W. Kim, J.N. Park, J.H. Cho, H.S. Kim, S.H. Paek, A fluorescent immunosensor for high-sensitivity cardiac troponin I using a spatially-controlled polymeric, nano-scale tracer to prevent quenching, Biosens. Bioelectron. 83 (2016) 19—26.

[14] H. Karimi-Maleh, F. Karimi, M. Alizadeh, A.L. Sanati, Electrochemical sensors, a bright future in the fabrication of portable kits in analytical systems, Chem. Rec. 20 (2020) 682—692.

[15] A. Khodadadi, E. Faghih-Mirzaei, H. Karimi-Maleh, A. Abbaspourrad, S. Agarwal, V.K. Gupta, A new epirubicin biosensor based on amplifying DNA interactions with polypyrrole and nitrogen-doped reduced graphene: experimental and docking theoretical investigations, Sensor. Actuator. B Chem. 284 (2019) 568—574.

[16] F. Tahernejad-Javazmi, M. Shabani-Nooshabadi, H. Karimi-Maleh, 3D reduced graphene oxide/FeNi3-ionic liquid nanocomposite modified sensor; an electrical synergic effect for development of tert-butylhydroquinone and folic acid sensor, Compos. B Eng. 172 (2019) 666—670.

[17] C. Karaman, O. Karaman, N. Atar, M.L. Yola, Electrochemical immunosensor development based on core-shell high-crystalline graphitic carbon nitride@carbon dots and Cd0.5Zn0.5S/d-Ti3C2Tx MXene composite for heart-type fatty acid-binding protein detection, Microchim Acta 188 (2021) 1—15.

[18] F. Ricci, G. Volpe, L. Micheli, G. Palleschi, A review on novel developments and applications of immunosensors in food analysis, Anal. Chim. Acta 605 (2007) 111—129.

[19] M.L. Yola, V.K. Gupta, T. Eren, A.E. Sen, N. Atar, A novel electro analytical nanosensor based on graphene oxide/silver nanoparticles for simultaneous determination of quercetin and morin, Electrochim. Acta 120 (2014) 204—211.

[20] V.K. Gupta, N. Atar, M.L. Yola, Z. Ustundag, L. Uzun, A novel magnetic Fe@Au core-shell nanoparticles anchored graphene oxide recyclable nanocatalyst for the reduction of nitrophenol compounds, Water Res. 48 (2014) 210—217.

[21] Q.Q. Zhang, Y.Y. Huang, B.Y. Jiang, Y.J. Hu, J.J. Xie, X. Gao, et al., In situ synthesis of magnetic mesoporous phenolic resin for the selective enrichment of glycopeptides, Anal. Chem. 90 (2018) 7357—7363.

[22] B.V.M. Silva, I.T. Cavalcanti, A.B. Mattos, P. Moura, M.D.T. Sotomayor, R.F. Dutra, Disposable immunosensor for human cardiac troponin T based on streptavidin-microsphere modified screen-printed electrode, Biosens. Bioelectron. 26 (2010) 1062—1067.

[23] Y. Chen, J.J. Feng, L.P. Mei, C.G. Shi, A.J. Wang, Dendritic core-shell rhodium@platinum-cobalt nanocrystals for ultrasensitive electrochemical immunoassay of squamous cell carcinoma antigen, J. Colloid Interface Sci. 555 (2019) 647—654.

[24] L.L. Li, G.H. Wu, G.H. Yang, J. Peng, J.W. Zhao, J.J. Zhu, Focusing on luminescent graphene quantum dots: current status and future perspectives, Nanoscale 5 (2013) 4015—4039.

[25] J.H. Shen, Y.H. Zhu, X.L. Yang, C.Z. Li, Graphene quantum dots: emergent nanolights for bioimaging, sensors, catalysis and photovoltaic devices, Chem. Commun. 48 (2012) 3686—3699.

[26] N. Ozcan, C. Karaman, N. Atar, O. Karaman, M.L. Yola, A novel molecularly imprinting biosensor including graphene quantum dots/multi-walled carbon nanotubes composite for interleukin-6 detection and electrochemical biosensor validation, ECS J Solid State Sc 9 (2020) 121010.

[27] C.A. Celaya, J. Muniz, L.E. Sansores, Theoretical study of graphyne-gamma doped with N atoms: the quest for novel catalytic materials, Fuel 235 (2019) 384—395.

[28] Y.Y. Sun, L. Chen, F.W. Zhang, D.Y. Li, H.Z. Pan, J. Ye, First-principles studies of HF molecule adsorption on intrinsic graphene and Al-doped graphene, Solid State Commun. 150 (2010) 1906—1910.

[29] X.R. Wang, X.L. Li, L. Zhang, Y. Yoon, P.K. Weber, H.L. Wang, et al., N-doping of graphene through electrothermal reactions with ammonia, Science 324 (2009) 768—771.

[30] B. Xu, Y.H. Lu, Y.P. Feng, J.Y. Lin, Density functional theory study of BN-doped graphene superlattice: role of geometrical shape and size, J. Appl. Phys. 108 (2010) 73711.

[31] M. Zhang, G.Y. Gao, A. Kutana, Y.C. Wang, X.L. Zou, J.S. Tse, et al., Two-dimensional boron-nitrogen-carbon monolayers with tunable direct band gaps, Nanoscale 7 (2015) 12023—12029.

[32] J. Mahmood, E.K. Lee, M. Jung, D. Shin, I.Y. Jeon, S.M. Jung, et al., Nitrogenated holey two-dimensional structures, Nat. Commun. 6 (2015) 6486.

[33] N.V.R. Nulakani, V. Subramanian, A theoretical study on the design, structure, and electronic properties of novel forms of graphynes, J. Phys. Chem. C 120 (2016) 15153—15161.

[34] M. Rafique, Y. Shuai, I. Ahmed, R. Shaikh, M.A. Tunio, Tailoring electronic and optical parameters of bilayer graphene through boron and nitrogen atom co-substitution; an ab-initio study, Appl. Surf. Sci. 480 (2019) 463—471.

[35] L. Ci, L. Song, C.H. Jin, D. Jariwala, D.X. Wu, Y.J. Li, et al., Atomic layers of hybridized boron nitride and graphene domains, Nat. Mater. 9 (2010) 430—435.

[36] J.F. Ni, Functional materials for next-generation rechargeable batteries, Funct Mater Lett 11 (2018) 1802001.

[37] F. Perreault, A.F. de Faria, M. Elimelech, Environmental applications of graphene-based nanomaterials, Chem. Soc. Rev. 44 (2015) 5861−5896.

[38] H. Wang, X.Z. Yuan, Y. Wu, G.M. Zeng, W.G. Tu, C. Sheng, et al., Plasmonic Bi nanoparticles and BiOCl sheets as cocatalyst deposited on perovskite-type ZnSn(OH)(6) microparticle with facet-oriented polyhedron for improved visible-light-driven photocatalysis, Appl. Catal. B Environ. 209 (2017) 543−553.

[39] H. Wang, Q.X. Mu, K. Wang, R.A. Revia, C. Yen, X.Y. Gu, et al., Nitrogen and boron dual-doped graphene quantum dots for near-infrared second window imaging and photothermal therapy, Appl Mater Today 14 (2019) 108−117.

[40] M.L. Yola, N. Atar, M.S. Qureshi, Z. Ustundag, A.O. Solak, Electrochemically grafted etodolac film on glassy carbon for Pb(II) determination, Sensor. Actuator. B Chem. 171 (2012) 1207−1215.

[41] R.Q. Feng, K.X. Tian, Y.F. Zhang, W. Liu, J.L. Fang, M.S. Khan, et al., Recognition of M2 type tumor-associated macrophages with ultrasensitive and biocompatible photoelectrochemical cytosensor based on Ce doped SnO2/SnS2 nano heterostructure, Biosens. Bioelectron. 165 (2020) 112367.

[42] B. Jeong, R. Akter, O.H. Han, C.K. Rhee, M.A. Rahman, Increased electrocatalyzed performance through dendrimer-encapsulated gold nanoparticles and carbon nanotube-assisted multiple bienzymatic labels: highly sensitive electrochemical immunosensor for protein detection, Anal. Chem. 85 (2013) 1784−1791.

[43] M.L. Yola, N. Atar, Development of cardiac troponin-I biosensor based on boron nitride quantum dots including molecularly imprinted polymer, Biosens. Bioelectron. 126 (2019) 418−424.

[44] Y. Yamada, K. Murota, R. Fujita, J. Kim, A. Watanabe, M. Nakamura, et al., Subnanometer vacancy defects introduced on graphene by oxygen gas, J. Am. Chem. Soc. 136 (2014) 2232−2235.

[45] M.L. Yola, N. Atar, Simultaneous determination of beta-agonists on hexagonal boron nitride nanosheets/multi-walled carbon nanotubes nanocomposite modified glassy carbon electrode, Mater Sci Eng C Mater Biol Appl 96 (2019) 669−676.

[46] Y.C. Zhang, Z.N. Du, K.W. Li, M. Zhang, D.D. Dionysiou, High-performance visible-light-driven SnS2/SnO2 nanocomposite photocatalyst prepared via in situ hydrothermal oxidation of SnS2 nanoparticles, Acs Appl Mater Inter 3 (2011) 1528−1537.

[47] M.L. Yola, N. Atar, Amperometric galectin-3 immunosensor-based gold nanoparticle-functionalized graphitic carbon nitride nanosheets and core-shell Ti-MOF@COFs composites, Nanoscale 12 (2020) 19824−19832.

[48] H. Medetalibeyoglu, M. Beytur, O. Akyildirim, N. Atar, M.L. Yola, Validated electrochemical immunosensor for ultra -sensitive procalcitonin detection: carbon electrode modified with gold nanoparticles functionalized sulfur doped MXene as sensor platform and carboxylated graphitic carbon nitride as signal amplification, Sensor. Actuator. B Chem. 319 (2020) 128195.

[49] L.X. Lin, S.W. Zhang, Creating high yield water soluble luminescent graphene quantum dots via exfoliating and disintegrating carbon nanotubes and graphite flakes, Chem. Commun. 48 (2012) 10177−10179.

[50] Y.Q. Dong, C.Q. Chen, X.T. Zheng, L.L. Gao, Z.M. Cui, H.B. Yang, et al., One-step and high yield simultaneous preparation of single- and multi-layer graphene quantum dots from CX-72 carbon black, J. Mater. Chem. 22 (2012) 8764−8766.

[51] J. Ristein, R.T. Stief, L. Ley, W. Beyer, A comparative analysis of a-C : H by infrared spectroscopy and mass selected thermal effusion, J. Appl. Phys. 84 (1998) 3836−3847.

[52] M. Bayle, N. Reckinger, J.R. Huntzinger, A. Felten, A. Bakaraki, P. Landois, et al., Dependence of the Raman spectrum characteristics on the number of layers and stacking orientation in few-layer graphene, Phys. Status Solidi B 252 (2015) 2375−2379.

[53] A.C. Ferrari, J.C. Meyer, V. Scardaci, C. Casiraghi, M. Lazzeri, F. Mauri, et al., Raman spectrum of graphene and graphene layers, Phys. Rev. Lett. 97 (2006) 187401.

[54] H.L. Fei, R.Q. Ye, G.L. Ye, Y.J. Gong, Z.W. Peng, X.J. Fan, et al., Boron- and nitrogen-doped graphene quantum dots/graphene hybrid nanoplatelets as efficient electrocatalysts for oxygen reduction, ACS Nano 8 (2014) 10837−10843.

[55] C. Karaman, O. Karaman, N. Atar, M.L. Yola, Tailoring of cobalt phosphide anchored nitrogen and sulfur co-doped three dimensional graphene hybrid: boosted electrocatalytic performance towards hydrogen evolution reaction, Electrochim. Acta 380 (2021) 138262.

[56] R.Z. Zhang, W. Chen, Nitrogen-doped carbon quantum dots: facile synthesis and application as a "turn-off" fluorescent probe for detection of Hg2+ ions, Biosens. Bioelectron. 55 (2014) 83−90.

[57] G. Eda, Y.Y. Lin, C. Mattevi, H. Yamaguchi, H.A. Chen, I.S. Chen, et al., Blue photoluminescence from chemically derived graphene oxide, Adv. Mater. 22 (2010) 505−509.

[58] L.B. Tang, R.B. Ji, X.M. Li, G.X. Bai, C.P. Liu, J.H. Hao, et al., Deep ultraviolet to near-infrared emission and photoresponse in layered N-doped graphene quantum dots, ACS Nano 8 (2014) 6312−6320.

[59] T. Kunyapat, F. Xu, N. Neate, N. Wang, A. Sanctis, S. Russo, et al., Ce-Doped bundled ultrafine diameter tungsten oxide nanowires with enhanced electrochromic performance, Nanoscale 10 (2018) 4718−4726.

[60] H. Vrubel, D. Merki, X.L. Hu, Hydrogen evolution catalyzed by MoS3 and MoS2 particles, Energy Environ. Sci. 5 (2012) 6136−6144.

[61] A.M. Santos, A. Wong, T.M. Prado, E.L. Fava, O. Fatibello, M.D.P.T. Sotomayor, et al., Voltammetric determination of ethinylestradiol using screen-printed electrode modified with functionalized graphene, graphene quantum dots and magnetic nanoparticles coated with molecularly imprinted polymers, Talanta 224 (2021) 121804.

[62] L.L. Yang, T.T. Wang, C.H. Bao, M. Shi, X.J. Huang, H. Cheng, A novel graphene quantum dots/choline chloride/gold nanoparticles-modified carbon fiber microelectrode for sensitive and selective determination of dopamine in the presence of a high concentration of ascorbic acid, J. Electroanal. Chem. 895 (2021) 115512.

[63] M. Khairy, B.G. Mahmoud, C.E. Banks, Simultaneous determination of codeine and its co-formulated drugs acetaminophen and caffeine by utilising cerium oxide nanoparticles modified screen-printed electrodes, Sensor. Actuator. B Chem. 259 (2018) 142−154.

[64] M. Yan, S. Feng, L. Yu, Y. Xue, J. Huang, X. Yang, Label-free immunosensor for cardiac troponin I detection based on aggregation-induced electrochemiluminescence of a distyrylarylene derivative, Biosens. Bioelectron. 192 (2021) 113532.

[65] H. Zhao, X. Du, H. Dong, D. Jin, F. Tang, Q. Liu, et al., Electrochemical immunosensor based on Au/Co-BDC/MoS2 and DPCN/MoS2 for the detection of cardiac troponin I, Biosens. Bioelectron. 175 (2021) 112883.

[66] X.J. Liao, H.J. Xiao, J.T. Cao, S.W. Ren, Y.M. Liu, A novel split-type photoelectrochemical immunosensor based on chemical redox cycling amplification for sensitive detection of cardiac troponin I, Talanta 233 (2021) 122564.

[67] D.X. Du, J.N. Shu, M.Q. Guo, M.A. Haghighatbin, D. Yang, Z.P. Bian, et al., Potential-Resolved differential electrochemiluminescence immunosensor for cardiac troponin I based on MOF-5-wrapped CdS quantum dot nanoluminophores, Anal. Chem. 92 (2020) 14113−14121.

[68] J.W. Zhao, J.W. Du, J.H. Luo, S.H. Chen, R. Yuan, A novel potential-resolved electrochemiluminescence immunosensor for the simultaneous determination of brain natriuretic peptide and cardiac troponin I, Sensor. Actuator. B Chem. 311 (2020) 127934.

[69] D.W. Fan, X. Liu, X.R. Shao, Y. Zhang, N. Zhang, X.Y. Wang, et al., A cardiac troponin I photoelectrochemical immunosensor: nitrogen-doped carbon quantum dots-bismuth oxyiodide-flower-like SnO2, Microchim Acta 187 (2020) 332.

[70] J.Y. Lim, S.S. Lee, Quartz crystal microbalance cardiac Troponin I immunosensors employing signal amplification with TiO2 nanoparticle photocatalyst, Talanta 228 (2021) 122233.